Delft University of Technology

Computational Ultrasound Carotid Artery Imaging with a Few Transceivers
An Emulation Study

Hu, Yuyang; Dogan, Didem; Brown, Michael; Leus, Geert; Steen, Antonius F.W.van der; Kruizinga, Pieter; Bosch, Johannes G.

Important note
To cite this publication, please use the final published version (if applicable).
Please check the document version above.

Computational Ultrasound Carotid Artery Imaging With a Few Transceivers: An Emulation Study

Yuyang Hu, *Student Member, IEEE*, Didem Dogan, *Member, IEEE*, Michael Brown, *Member, IEEE*,
Geert Leus, *Fellow, IEEE*, Antonius F. W. van der Steen, *Fellow, IEEE*,
Pieter Kruizinga, *Member, IEEE*, and Johannes G. Bosch, *Member, IEEE*

Abstract—Ultrasonography could allow operator-independent examination and continuous monitoring of the carotid artery (CA) but normally requires complex and expensive transducers, especially for 3-D. By employing computational ultrasound imaging (cUSi), using an aberration mask and model-based reconstruction, a monitoring device could be constructed with a more affordable simple transducer design comprising only a few elements. We aim to apply the cUSi concept to create a CA monitoring system. The system's possible configurations for the 2-D imaging case were explored using a linear array setup emulating a cUSi device in silico, followed by in vitro testing and in vivo CA imaging. Our study shows enhanced reconstruction performance with the use of an aberrating mask, improved lateral resolution through proper choice of the mask delay variation, and more accurate reconstructions using least-squares with QR (LSQR) decomposition compared to matched filtering (MF). Together, these advancements enable B-mode reconstruction and power Doppler imaging (PDI) of the CA with sufficient quality for monitoring using a configuration of 12 transceivers coupled with a random aberration mask with a maximum delay variation of four wave periods (WPs).

Index Terms— B-mode imaging, carotid artery (CA), computational ultrasound imaging (cUSi), emulation, monitoring, power Doppler imaging (PDI), ultrasonography.
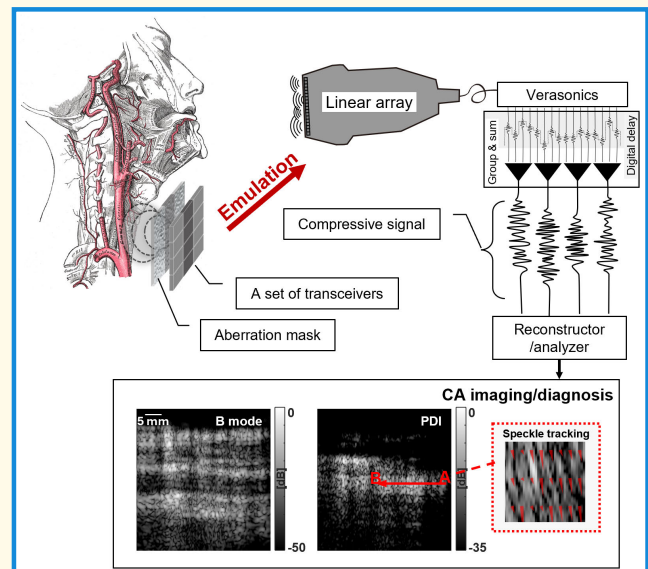
I. INTRODUCTION

ULTRASONOGRAPHY provides a real-time and noninvasive way to image human anatomy and derive functional

information. The carotid artery (CA) is very accessible for ultrasonic examination of the vessel anatomy, blood velocity, flow profile, wall motion, and pulse wave velocity (PWV). These can be used to diagnose stenosis, atherosclerosis, hypertension, and so on [1], [2], [3], [4] and could, in principle, also be useful for the long-term monitoring of such processes. The examination is normally performed by a skilled sonographer using an ultrasound system with a linear array transducer, which requires considerable anatomical knowledge and probe manipulation to acquire the best possible 2-D image. Having out-of-plane [5] or 3-D imaging capabilities would allow more detailed functional assessment with a less critical transducer placement and might offer possibilities for repeated assessments or continuous monitoring without a skilled operator [6], [7]. However, a fully populated 3-D ultrasound matrix array requires complex fabrication and high-end electronics, making it costly and less accessible for routine monitoring [8], [9]. To reduce system complexity and cost, we aim to simplify the probe design by minimizing the number of elements while preserving imaging quality despite fewer measurements and

Highlights

- **A novel cUSi method using a few transceivers and an encoding mask is introduced for CA monitoring.**

- **Our study shows that 12 transceivers with a random aberration mask (four WPs' delay variation) are sufficient for 2-D B-mode and PDI of the CA.**

- **This research provides useful configurations for 2-D cUSi of the CA that indicates a direction toward affordable, simple 3-D monitoring.**

lower spatial sampling. Ultimately, our goal is to develop a simpler, low-cost, and operator-independent 3-D ultrasound system for CA monitoring.

In a previous study, Kruizinga et al. [10] proposed a computational imaging-based method using a single-element sensor for 3-D imaging. By placing a coded aperture mask in front of the sensor, a spatially encoded acoustic field was generated that allowed detailed 3-D reconstructions of complex 3-D objects from a limited number of observations. The feasibility of such a computational ultrasound imaging (cUSi) approach in 4-D visualization of mouse brain hemodynamics has been validated in our group's recent work [11], as well as in other applications [12], [13]. However, much remains to be investigated for these methods, especially when configuring it for a specific application, regarding mask characteristics, number of transceivers, and number of observations.

We intend to use the cUSi concept to develop a device for CA monitoring. However, since there is limited insight into the properties of sensor configurations that can work well in a specific application, it is inefficient to immediately embark on the development of an actual device prototype. With the large number and range of undetermined parameters, it is even challenging to perform simulations for this development over a large parameter space. Therefore, we first want to explore the possibilities for a predetermined setup and a limited range of a few main parameters, allowing both efficient simulation and experimental validation using an emulation approach. We expect this emulated device to provide distinguishable anatomical CA structures—including the vessel wall, lumen, and surrounding tissue—ideally with an image quality approaching conventional imaging methods. Our study only focuses on its 2-D imaging potential in this article, assuming that similar parameters could be used for extension to 3-D scenarios.

In this article, we describe the cUSi concept and our emulation setup in more detail and perform simulations on the expected B-mode imaging performance, in vitro experiments on the imaging of a phantom, and, finally, B-mode and power Doppler imaging (PDI) reconstructions from in vivo measurements with the emulation system on a volunteer's CA. The feasibility of our cUSi implementation is demonstrated, and two reconstruction schemes for the compressed signals are compared. The effect of different mask and transceiver configurations on the reconstruction quality is studied. The results supply a lower limit for the number of transceivers in a practical device design sufficient to separate functional information spatially.

II. METHODS

### A. Emulation of a cUSi Device

As illustrated in Fig. 1(a), the proposed cUSi device for CA monitoring will employ a small number of large transceivers with aberration masks arranged longitudinally along the CA. This arrangement allows each transceiver to capture information from a large part of the field of view. Using aberration masks on these transceivers is a critical feature of the cUSi method. Although aberration is typically unwanted and considered detrimental to image quality, in our approach, it serves as a controlled encoding technique—since it is precomputed or measured—to address the spatial resolution limitations of systems with fewer, larger transceivers. Masks with irregular aberration patterns generate a complex, diverging acoustic field, where each spatial location receives a distinct signal. This structured field plays a crucial role in enhancing spatial resolution and effectively separating signals in spatially under-sampled transceiver configurations. To achieve useful imaging of the CA field of view, a device aperture of about 4 cm and an imaging frequency within the range of 5–8 MHz are adopted, similar to what is generally used for carotid imaging.

In this emulation, as shown in Fig. 1(b), transducer elements were given an individual delay and were grouped to represent the larger transceivers. The individual elements' delayed radio frequency (RF) signals were summed to represent the single transceiver signal that will be used for image reconstruction. The local delay induced by a physical aberration mask, causing phase shift and interference to the acoustic wavefront, was translated into spatially discretized digital delays applied per element of the linear array [Fig. 1(c)]. For simplification, other effects of the mask, such as material attenuation, internal reflection, and surface waves, were ignored in this emulation. Furthermore, the digital delay was quantized spatially (because of the transducer element size), possibly leading to deviations. Therefore, we will need to verify whether the acoustic field of the physical mask and the emulated situation match sufficiently.

B. System Setup for Emulation Experiments and Simulations

For the emulation system, we used a 128-element linear array transducer (L7-4, ATL, Philips Healthcare, Cambridge, MA, USA) suitable for CA imaging and a Vantage 256 research ultrasound system (Verasonics Inc., Kirkland, WA, USA), allowing full control over each element's transmission and access to all received element RF signals. One fixed delay value per transducer element was used in the Verasonics
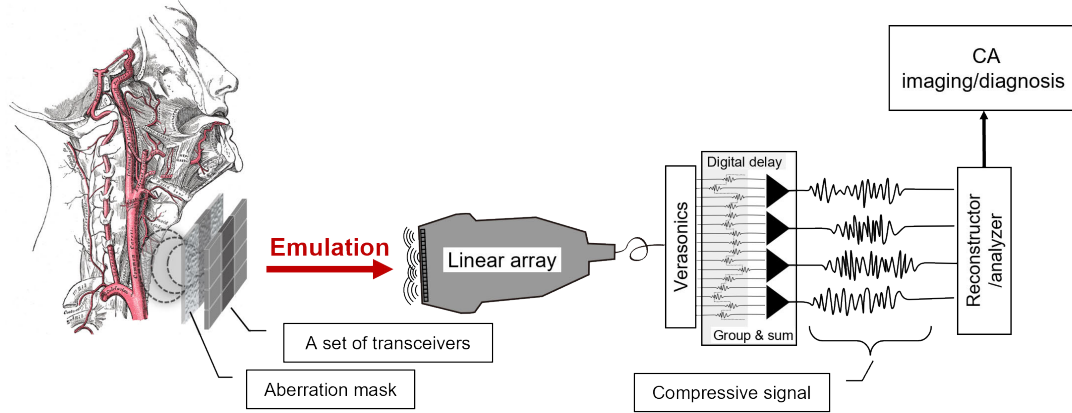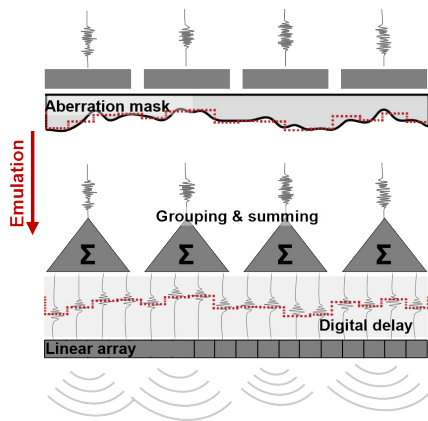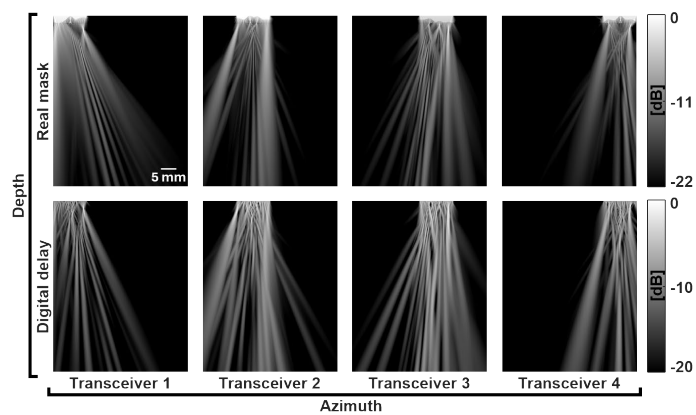
Fig. 1. (a) Intended practical device. Signals are acquired by a transceiver matrix array with mask. One row of such a matrix array was emulated in our study. In this example, the row has four transceivers. (b) Emulation system scheme. The red dotted line is the per-element delay pattern discretized from a smooth, continuous physical aberration mask. Transmitted and received signals from a linear array are delayed and summed per group according to this pattern. (c) k-Wave simulated field for a four-transceiver configuration from a physical mask (upper row) and a digital delay mask (bottom row) is visually very similar.

system to emulate the physical mask's local delaying effect in transmit and receive. Since we want to compare the effect of different combinations of parameters, we chose to use the same mask pattern for all experiments. We are aware that this choice implies some local effects on the reconstruction quality, which will be addressed in the following research stage.

A 1-D mask pattern was first simulated at a step of 50 μm with a normalized, random, and uniform thickness distribution over an aperture of 39.4 mm, equal to the aperture of the L7-4 linear array we used from emulation. This pattern was then smoothed by applying a Gaussian-weighted average within a moving window of 3 mm to be more realistic for manufacturing and eventually discretized into 128-element delays. Although our earlier work [12] indicated that this random mask already provides good results, it can still be optimized in a later stage for a further limited improvement in image reconstruction.

In the context of emulation, the term *transceiver* in this article explicitly refers to such a group of linear array elements of which the signals are combined into a single entity. Note that beamforming effects, such as the effective directivity of the grouped elements in the transceiver, will be automatically

handled by our model-based reconstruction where first-order acoustic wave propagation effects are adequately modeled. When an even division of the 128 elements was not applicable, the remaining elements at the right end of the transducer were omitted.

For the 2-D simulations, we employed k-Wave, a widely used open-source time-domain simulation toolbox for the propagation of acoustic waves [14], where the transducer definition is that of the L7-4 used in the emulation system. Additionally, a physical mask composed of TPX and silicone rubber layers was simulated and coupled to the transducer. The local thickness of each material was calculated from the desired local delay, and the encoded acoustic fields generated were compared to those generated by digital delays. The detailed simulation parameters used in k-Wave are listed in Supplementary Table SI.

C. cUSi System Model

For a regular array where the geometry uniquely defines the image reconstruction problem, simple algorithms like delay-and-sum can be used [15]. For our situation, we require a

more complex model-based reconstruction approach that links each voxel's interaction with the spatially varying field with each transceiver output [10], [15]. In this model-based reconstruction, the imaging system is described as a linear model $y = Ax$, where y is the set of received transceiver signals, which is denoted as the product of a system matrix A and the ground truth spatial scatterer distribution x, representing the scattering strength at each spatial position (x, z) in a discretized region of interest (ROI) of size $N_x \times N_z$. The system matrix A contains the pulse-echo responses representing element signals of each pair of transmit and receive elements associated with each possible position (x, z) of a scatterer. Thus, the received signals are modeled as the linear sum of the scattered responses of all scatterers. If the pulse-echo responses are sufficiently unique and/or the number of observed element signals is large enough, the spatial scatterer distribution can be reconstructed from the received signals with reasonable spatial separation by a pseudoinverse relation, represented by $x = A^\dagger y$. In this article, we will employ two methods to approximate/regularize the pseudoinverse, namely matched filtering (MF) and least squares with QR (LSQR) decomposition, both described next.

In describing our emulation system on a transducer with E elements, the linear model is detailed as follows:

$$y_{(n_t, n_r)}(t) = \sum_{x=1}^{N_x} \sum_{z=1}^{N_z} A_{(n_t, n_r)}(t, x, z) \times x(x, z). \quad (1)$$

This model relates $y_{(n_t, n_r)}$, the received signal of the element n_r following transmission on the element n_t, to x, the backscattering intensity of the distributed scatterers via matrix A. Here, $n_t, n_r \in \{1, 2, \ldots, E\}$. Applying the principle of reciprocity, i.e., each element's identical behavior during transmission and reception, the pulse-echo response is formulated within matrix A by convoluting the transmitting and receiving element's forward pressure.

In this article, we modeled the forward pressure field by applying the one-way element response of the L7-4 transducer, as predicted by the Verasonics Vantage simulator, to the k-Wave simulated element array, using it as the normalized time-varying particle velocity in the depth direction. A single element's general 2-D pressure field was generated, assuming that all elements' pressure fields are identical, except for spatial translation and time delay.

For our emulation, individual elements are grouped into M transceivers. The linear system model remains similar, but now, y and A are constructed per transceiver. Assuming synthetic aperture (SA) transmission per transceiver (s_t) and reception on each transceiver (s_r), we derive this new equation

$$y_{(s_t, s_r)}(\omega) = \sum_{x=1}^{N_x} \sum_{z=1}^{N_z} A_{(s_t, s_r)}(\omega, x, z) \times x(x, z) \quad (2)$$

where $y_{(s_t, s_r)}$ and $A_{(s_t, s_r)}$ represent the summed transceiver signals and pulse-echo response matrix of all elements in each transceiver, respectively, and $s_t, s_r \in \{1, 2, \ldots, M\}$. Note that this model is also converted to the frequency domain for simplicity in actual manipulation, such as frequency-domain-based downsampling and convolution. The frequency signal ω

is obtained through the Fourier transform of the time-domain signals y and A.

D. Simulations and Experiments

In the context of a practical cUSi system configuration, we focus on two key parameters for our study. The first parameter is the number of transceivers M, which is directly related to the overall complexity of cabling and signal processing in the final system setup. The second parameter is the mask delay variation factor D, which was used to scale the normalized random mask pattern and to adjust the heterogeneity of the pulse-echo responses in the system matrix A, which is expected to play a crucial role in reconstruction performance. We noted the mask delay variation factor in the unit of wave periods (WPs) of the driving frequency, e.g., $D = 4$ WP at 5 MHz corresponds to a delay range of 0.8 μs.

By adjusting these two parameters M and D, we aim to optimize the balance between system complexity and imaging performance in the cUSi system.

We started our study with a simulation on an in silico model, where nine scatterers were evenly distributed in a 40×50 mm ROI [shown in Fig. 2(a)], typical for CA imaging. Simulation parameters are listed in Table SI. The point spread function (PSF) and contrast ratio (CR) were evaluated for different M and D combinations using MF reconstruction. We simulated the transducer array excited at 5 MHz with a four-cycle tone burst pulse, as we applied in the in vitro and in vivo experiments. Echoes from the scatterers across all 128 elements were captured in an SA transmit fashion [16], and since under the assumption of linearity, we can construct any transceiver transmit and receive signal from combinations of element transmit and receive signals with the proper delays applied. These SA signals were subjected to varying element time delays and grouped, representing combinations of different numbers of transceivers and mask delay variations. We simulated increasing numbers of transceivers ($M = 1$, 2, 4, 8, and 16) from a single large-aperture transceiver to 16 smaller aperture transceivers. D was varied over 0, 1, 2, 4, 8, 16, and 32 WP, representing scenarios from no mask to very thick masks, creating increasingly heterogeneous acoustic fields. Consecutively, a more detailed examination of the part of this parameter space that proved most relevant was conducted, specifically exploring M between 8 and 16 (in increments of 2) and D between 4 and 16 WP (also in increments of 2).

For the in vitro emulation experiments, we employed a tissue-mimicking phantom (CIRS model 040GSE, Norfolk, VA, USA) and acquired the RF element signals in a synthetic transmit aperture fashion (transmit on one element, receive on all) over a depth range of 5–50 mm, in line with our in silico model. The transmission repetition frequency was set to 8 kHz, close to the highest frequency we could achieve with our Verasonics system for this depth. In the reconstructions, we could generate any cUSi configuration in retrospect by applying proper delays and combining signals. A 128-transceiver emulation with no mask delay was also reconstructed as ground truth, which is equivalent to the standard SA delay and sum
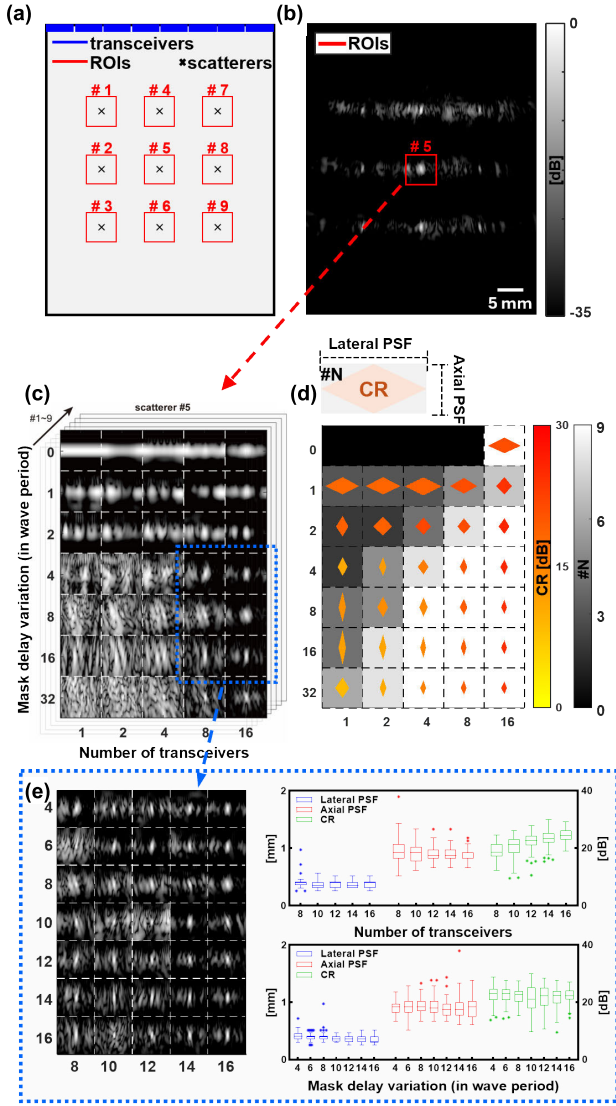
Fig. 2. In silico study on nine scatterers. (a) Geometry of simulation setup, overlaid with nine ROIs for PSF analysis. (b) Reconstruction of 16-sensor emulation with eight WP mask delay variation. (c) Reconstruction of scatterer #5 (center of 9) for all parameter combinations. (d) Averaged PSF of all nine scatterers for all parameter combinations. Lateral PSF improved for higher mask delay variation. Axial PSF and CR improved for a higher number of transceivers. (e) Exploring parameters in a finer step. Configurations between 4–16 WP and 8–16 transceivers were checked. Scatterer reconstruction is less sensitive to the mask delay variation than to a number of transceivers. The numerical results of (d) and (e) are reported in Supplementary Tables SII and SIII.

(SA-DAS) method. In the reconstructions, we chose $M = 16$ and $D = 8$ (which performed well in the in silico study) to achieve a proper MF reconstruction. We compared it to an LSQR reconstruction and also to MF and LSQR reconstructions for the case of no mask ($D = 0$). Based on the best combination, we also tried with lower M, to see how much the image quality would degrade using less transceivers.

Finally, we used this emulation system to image the CA in a healthy volunteer, employing both B-mode imaging and power Doppler flow detection. This in vivo study was approved by the local medical ethics committee (Erasmus MC MEC-2014-611), and the volunteer also provided informed consent. Since

this is a moving object, a full SA acquisition is too slow for useful cUSi reconstruction because the motion will change the image ($\boldsymbol{x}$) considerably over the transmissions. Therefore, we apply one transmit for each transceiver, with actual transmit delays applied to all elements in the transceiver group. Transceivers were excited at a pulse repetition frequency of 8 kHz (actual frame rate = 8000/12), and data were acquired over 2 s for each imaging mode. Compared to the in vitro case, we aimed at a more practical configuration with low system complexity and relatively robust performance in a low signal-to-noise ratio (SNR) scenario. Therefore, we emulated a probe with even fewer transceivers and a thinner mask ($M = 12$ and $D = 4$ WP). We also compared it to a 12-transceiver probe without a mask. For comparison to classical imaging, we acquired a 12-angle (within $\pm 5°$) compound plane wave imaging using all 128 elements. A 20-mm-thick gel pad was used as a standoff in these experiments, targeting an ROI with optimal image quality for in vivo CA imaging at 25–50 mm depth, where a more uniform pressure distribution is present because of the diverging acoustic field propagation.

E. Reconstruction

1) Data Preparation: In this study, most of the signal processing, including the design of the model matrix, was done in the frequency domain using frequencies between 3.7 and 6.7 MHz (58% bandwidth).

2) MF Method: A regular matrix inversion is not feasible due to the highly underdetermined nature of the problem ($M^2 \times n_\omega \ll N_x N_z$). Therefore, we turn to an MF reconstruction as our fundamental approach [17], which can provide an approximation of $\boldsymbol{x}$. The MF method was implemented as follows:

$$\hat{\boldsymbol{x}}_{\mathrm{MF}} = \sum_{s_t=1}^{M} \sum_{s_r=1}^{M} \left(A_{(s_t,s_r)}^H \boldsymbol{y}_{(s_t,s_r)} \right). \tag{3}$$

In this method, the Hermitian matrix $\boldsymbol{A}^H$ serves as an approximation of the pseudoinverse of $\boldsymbol{A}$, bypassing the challenges of direct matrix inversion. This approach is robust and relatively fast, notably reducing the computational time required for obtaining other pseudoinverse matrices. The MF method was applied to signals from each pair of transmit and receive transceivers individually (SA per transceiver), enhancing reconstruction quality by maximizing the number of observations. These observations were then aggregated to provide $\hat{\boldsymbol{x}}_{\mathrm{MF}}$ as an estimate of the actual $\boldsymbol{x}$ vector. It should be noted that since this is not a true inversion, the MF reconstruction will not fully compensate for intensity variations resulting from the patterned acoustic field.

3) Least Squares With QR Decomposition: To overcome the limitations of the MF method, we also explored a regression-based approach named LSQR (LSQR decomposition) [18]

$$\min \left\| \sum_{s_t=1}^{M} \sum_{s_r=1}^{M} \left(A_{(s_t,s_r)} \hat{\boldsymbol{x}}_{\mathrm{LSQR}} - \boldsymbol{y}_{(s_t,s_r)} \right) \right\|_2. \tag{4}$$

This method involves an iterative minimization of the general error between $A_{(s_t,s_r)} \hat{\boldsymbol{x}}_{\mathrm{LSQR}}$ and $\boldsymbol{y}_{(s_t,s_r)}$ across all observations

and eventually finds an estimate $\hat{x}_{\text{LSQR}}$ that is closer to the actual x. While this method is time-consuming, it yields a more precise reconstruction. In our implementation, the regularization process was terminated after five iterations. Empirically, we observed that further iterations beyond this point did not considerably enhance image quality.

4) Power Doppler Imaging [19]: In our in vivo CA experiment, we reconstructed power Doppler images to assess the emulation system's efficacy in depicting blood flow. To mitigate the impact of vascular wall motion on our results, we only processed B-mode data captured during the diastolic phase of the cardiac cycle. Before executing PDI, singular value decomposition (SVD) was applied with a manually determined rank threshold cutoff as a clutter filter. This approach effectively suppressed signals from the vascular wall and other semi-stationary tissues [20].

F. Evaluation

To evaluate the performance impact of the number of transceivers, mask delay variation, and reconstruction methods in our emulation system, we focused on spatial separability. This was assessed in terms of lateral and axial PSF, determined as the full-width at half-maximum (FWHM) of the response at each scatterer, and the CR between object and background intensity, defined as

$$\text{CR} = 20 \times \log_{10}\left(\frac{\text{rms(object)}}{\text{rms(background)}}\right) \quad (5)$$

where $\text{rms}(\cdot)$ corresponds to the square root of the mean of squared intensities within the respective area. For the in silico case, we reconstructed images for all parameter combinations using MF. We chose not to use LSQR in this in silico study, as it may easily obtain a close-to-perfect reconstruction of this sparse scatterer distribution, whereas such distributions do not exist in reality. Moreover, we selected nine 5×5 mm ROIs centered around the ground truth scatterers' positions (marked by red boxes in Fig. 2). A 3×3 pixel region at the center of each ROI was designated as the object area, with the remaining pixels serving as the background for CR calculations. The PSF in these ROIs was individually normalized to the intensity at the center sample point. The FWHM was calculated with respect to the intensity of the central pixel in the ROI, rather than the peak intensity, since this was sometimes located off-center. In some reconstructions such as the top row of Fig. 2(c), the PSF was deemed unsuitable for evaluation. Reconstructions were automatically marked as invalid and excluded from further evaluation if:

1) The PSF extended beyond the edges of the ROI and
2) The peak intensity was not at the center pixel and was more than 6 dB stronger than the center pixel.

Note that this approach in borderline cases may accept scatterer reconstructions that are visually poorly recognizable, and therefore, the PSF analysis might be somewhat biased.

In the in vitro experiment, a similar approach was used for calculating PSFs in eight ROIs (red boxes in Figs. 3 and 4). However, the CR, in this case, was derived from the comparison of an echogenic inclusion to a corresponding background region [green dashed circles in Figs. 3(a)
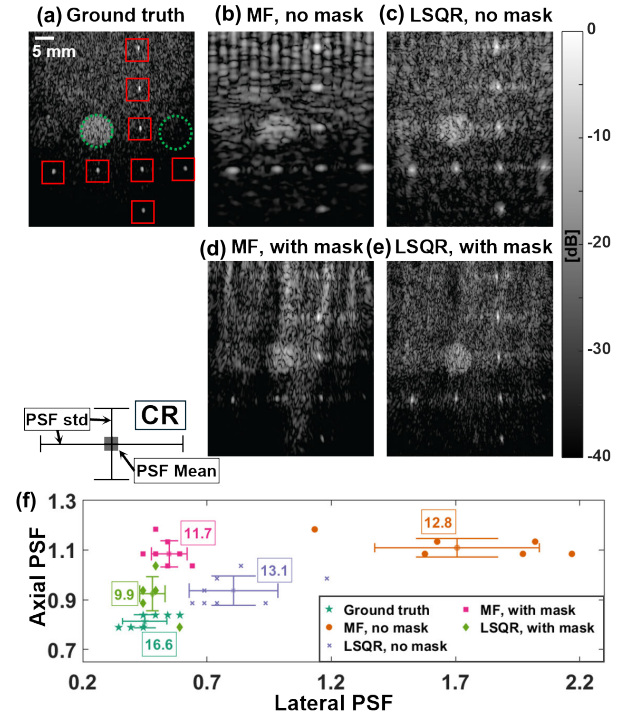

Fig. 3. Comparison of in vitro image reconstructions of CIRS phantom for different methods. (a) MF reconstruction with 128 transceivers' signals without mask (ground truth). (b)–(e) Reconstruction from 16 transceivers by different schemes: (b) MF without mask, (c) LSQR without mask, (d) MF with mask, and (e) LSQR with mask. FWHM of PSF was determined for the red boxes and CR from the green circles. (f) Overview of results, LSQR with mask provides the best reconstruction. The numerical results of (f) are reported in Table I.

and 4(a)]. We compared the reconstruction performance of four combinations of reconstruction cases (with/without mask and with MF/LSQR). The significances of these combinations' performance differences were tested through a paired Student's t-test.

For the in vivo CA validation experiment, we evaluated the effects of MF and LSQR for the B-mode and PDI reconstructions derived from the longitudinal view of a common CA (CCA). To assess the system's capability for flow sensing, we analyzed the speckle pattern along an anatomical M-mode line within the vessel lumen's center from the PDI reconstruction (Fig. 5(a), red line). Moving speckles appear as diagonal stripes in this M-mode figure, representing their varying positions at the center of the lumen over different slow-time frames. The slope of each stripe corresponds to the speed of the speckle movement. A 1-D speckle tracking was employed [21], utilizing a template window of 2 mm, a searching window of 4 mm, and a step size of 0.27 mm to estimate local displacement along this line in the extracted M-mode image.

III. RESULTS

A. Validity of Digital Delay Emulation

Fig. 1(c), bottom, shows the encoding field pattern generated by a four-transceiver emulation system with digital delays. These fields demonstrated a clear qualitative similarity to the

TABLE I
FWHM OF PSF [MEAN (±SD)] AND CR FROM IN VITRO PHANTOM EXPERIMENT

Reconstruction schemes		no mask		with mask				
Number of transceivers		128 (GT)	16	16	14	12	10	8
MF	Lateral PSF [mm]	0.39(±0.1)	1.68(±0.34)	0.52(±0.07)*				
	Axial PSF [mm]	0.75(±0.04)	1.08(±0.05)	1.05(±0.06)				
	CR [dB]	16.64	12.85	11.73				
LSQR	Lateral PSF [mm]		0.78(±0.17)†	0.43(±0.06)*†	0.39(±0.1)	0.53(±0.13)	0.55(±0.15)	0.49(±0.08)
	Axial PSF [mm]		0.91(±0.05)†	0.89(±0.07)†	0.81(±0.15)	0.99(±0.12)	1.13(±0.24)	1.21(±0.31)
	CR [dB]		13.09	9.94	9.17	9.22	8.24	5.67

*significantly lower than no mask case * $p < 0.05$
†significantly lower than MF case † $p < 0.05$

simulation of transceivers coupled with a physically defined mask (Fig. 1(c), top), supporting the validity of emulating a physical mask by digital delays in cUSi.

B. In Silico Study of Nine Scatterers

Fig. 2 shows the results of the MF reconstruction of the in silico phantom with nine scatterers for different parameter combinations. Fig. 2(b) shows the distinct reconstruction of all nine scatterers for $M = 16$ and $D = 8$ WP, and Fig. 2(c) shows reconstructions for all combinations of M and D of the middle scatterer (#5). From the result #N, the number of markers that were considered valid, and it is clear that $D <= 2$ and $M <= 4$ do not provide acceptable results. #N is visualized by the background color in Fig. 2(d) (black = 0, all excluded; white = 9, none excluded). There was a clear improvement in reconstruction quality with increasing M and D. which was consistent as well across the average of all nine scatterers shown in Fig. 2(d). An increase in M, especially at higher D (4–32 WP), led to an improved axial PSF/resolution, likely enabled by the increased number of observations from different viewing angles and their additional phase and amplitude information from the region behind the scatterers. Similarly, the CR of the scatterers was found to increase as M increased. As D increased, the lateral PSF decreased, indicating a corresponding improvement in the system's lateral resolution, which flattens off beyond $D = 4$. This effect is linked to the fact that an aberration mask breaks the strong directivity (narrow opening angle) of large transceivers. Increasing D progressively weakens this directivity, allowing more transceivers to contribute signal information from a certain scatterer, thereby sharpening its PSF. However, beyond a certain point, this resolution gain is outweighed by an increase in clutter, which explains why the CR [represented by the color of the diamonds in Fig. 2(d)] initially improves but then deteriorates at a higher D. The best CR appeared at D of 2–4 WP, shown in the numerical results reported in Supplementary Table SII.

Apart from the above observations, in Fig. 2(b), it can be seen that scatterers in different positions have different intensities. We consider this an inherent limitation of MF, as its Hermitian matrix approach cannot correct for the uneven image intensity distribution caused by the nonuniform acoustic pressure distribution. Furthermore, the clutter levels of the three scatterers closest to the transducer (1, 4, 7) were stronger than those situated deeper. This difference is attributed to the inadequate overlap of transceiver fields in the shallower part of the ROI. Therefore, for optimal reconstruction quality, the ROI should preferably be positioned deeper from the transducer, possibly with the help of a standoff, as we did in the in vivo experiment. To better illustrate the spatial variations in reconstruction quality caused by the irregular acoustic field distribution, we provide Supplementary Fig. S1 showing full field-of-view reconstructions for $M = 4$ and $M = 16$.

To further localize the most useful parameter combinations, we performed a more detailed examination of the most promising parameter range using $M = 8$–16 transceivers and $D = 4$–16 WP [Fig. 2(e)]. For all parameter combinations, all nine scatterers were successfully reconstructed (except the #1 scatterer for $M = 12$ and $D = 10$ WP and visually sufficient results in similar quality were achieved. Only a minor improvement of CR was seen for a higher M (Fig. 2(e), top right) and lateral PSF for a higher D (Fig. 2(e), bottom right). The numerical results of this finer exploration are reported in Supplementary Table SIII.

Given the satisfactory reconstruction of the scatterers at 4–8 WP and considering that thicker masks in real life may imply higher attenuation and more severe internal reflections, we selected $D = 4$ WP and $M = 12$ transceivers for the volunteer in vivo studies. Especially for PDI, the attenuation from a thicker mask may be too restrictive. In the in vitro phantom study, we selected a more challenging setup with 8 WP and 16 transceivers, which provided the best spatial resolution by MF within the acceptable range of parameter combinations, to best evaluate the effects of LSQR.

C. In Vitro Imaging of CIRS Phantom

In our in vitro phantom imaging study, we observed that the reconstruction outcomes with various parameters closely align with those from the in silico study. Fig. 3 shows the MF and LSQR reconstruction results for the imaging with 16 transceivers, with or without an eight WP mask, in comparison to the ground truth (SA-DAS). Fig. 4 shows the results of LSQR reconstructions with mask for different numbers of transceivers M. Notably, comparing scenarios with and
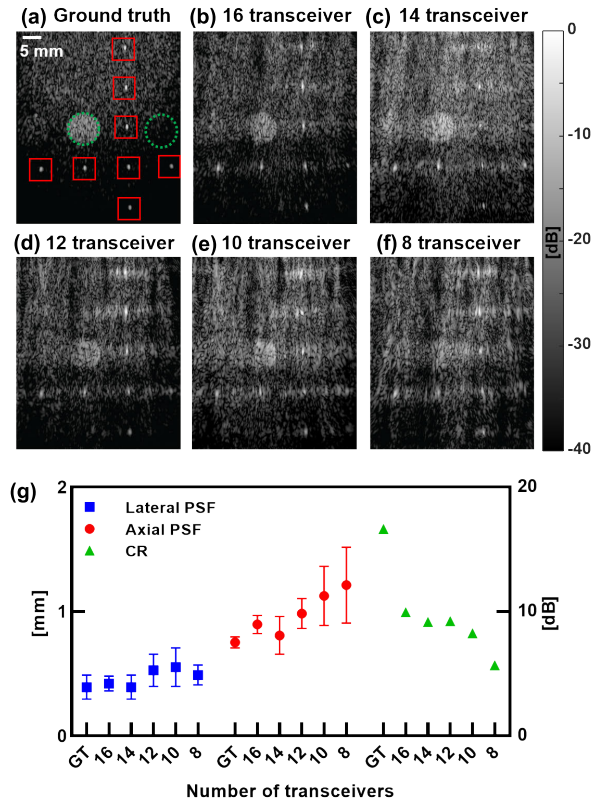
Fig. 4. Comparison of in vitro image reconstructions of CIRS phantom across varying number of transceivers. (a) MF reconstruction utilizing signals from 128 transceivers without a mask (ground truth). (b)–(f) Reconstructions for decreasing numbers of transceivers, ranging from 16 to 8, where both a mask and LSQR were applied. A gradual decline in reconstruction quality can be observed with a reduced number of transceivers and is shown quantitatively in graph (g) numerical results of (f) are reported in Table I.

without a mask, analogous to the in silico study, using a mask produced a marked improvement in lateral PSF [Fig. 3(b) versus (d) and (f)]. The enhancement in the axial PSF was particularly related to an increase in M (Fig. 4(g), red), which is also in line with the prior in silico study. Regarding CR, it was apparent that the clarity of the inclusion region improved with an increasing M (Fig. 4(g), green) and appeared independent of mask usage [Fig. 3(b) and (c) versus (d) and (e)]. Moreover, the visibility of wire targets, compared to inclusions, required fewer transceivers, with clear differentiation achievable with as few as eight transceivers [Fig. 4(f)].

This phantom experiment also involved a comparison of the reconstruction quality using MF and LSQR. LSQR notably improved image quality. In scenarios without a mask, LSQR also notably improved the lateral PSF [Fig. 3(b) versus (c)], a change observable both visually and statistically (Table I). Furthermore, LSQR brought about a modest enhancement in axial PSF. Second, LSQR produced a more balanced intensity distribution in the reconstruction [Fig. 3(c) and (e)]. MF reconstructions exhibited prominent brighter and darker stripes in the near field, and with a mask, even wire targets at identical depths display uneven intensities. As mentioned, these artifacts were caused by the irregular pressure field distribution, detailed in Supplementary Fig. S2(a).

The minimization approach of LSQR effectively mitigated this artifact [Fig. S2(b) versus (c)]. At the same time, this approach increased background clutter levels and the CR did not show improvement with LSQR.

Compared to the 128-transceiver ground truth, the 16-transceiver emulation setup using a mask and reconstruction via LSQR demonstrated the best overall reconstruction, particularly for PSF of wire targets, nearly reaching the ground truth level. Even at a reduced M of 12, the prominent features in the phantom, such as wire targets and inclusions, were distinctly visible. These numbers of transceivers ($M = 12$–16), therefore, were deemed suitable for our proposed application.

D. In Vivo Study of CA

In our in vivo experiment, utilizing a 12-transceiver emulation and D of 4 WP, we successfully reconstructed both the B-mode and PDI of the CCA of a healthy volunteer. We noted that applying a mask along with LSQR reconstruction resulted in a more detailed and continuous representation of the vessel's wall structure (Fig. 5(a), top). However, this improvement was relatively limited compared to the in vitro study, possibly due to small aberrations from the tissue introducing additional mismatches between the system model and the actual field [Fig. S2(d)], which affected the performance of LSQR reconstruction [Fig. S2(f)]. In the PDI observations, blood flow signals within the lumen were discernible across all cases. Nonetheless, the quality of blood flow speckles notably improved when the mask and LSQR were used (Fig. 5(a), bottom, 2nd versus 5th). This enhancement was evident when compared to the ground truth M-mode image (Fig. 5(b), 1st), containing distinct tilted stripe patterns indicative of local blood displacement (Fig. 5(b), 5th).

These high-resolution speckles offered a clearer depiction of blood flow dynamics. This was confirmed by displacement estimates obtained through 1-D speckle tracking, which closely matched the ground truth for the cases with mask (Fig. 5(c), 4th and 5th) but not in the cases without (Fig. 5(c), 2nd and 3rd). Furthermore, from the histogram analysis in Fig. 5(d), we observed that after applying the mask, the estimated velocity distribution shifts closer to the ground truth (0.19 ± 0.14 versus 0.31 ± 0.03), indicating an improvement in estimation accuracy. The erroneous peaks at both ends of the histogram that are caused by deficient speckle tracking remain included in the histogram for completeness.

IV. DISCUSSION

In this study, we investigated key system parameters for a cUSi system tailored to CA imaging, utilizing our innovative 2-D emulation framework. This exploration focused on the number of transceivers M, mask delay variation D, and the choice of reconstruction algorithm (MF versus LSQR). Our findings indicate that, as expected, reconstruction quality improves for an increased M, enhancing both the axial PSF and the CR. Increasing D generally led to a narrower lateral PSF. This improvement is in correspondence with what has been reported in [10]. Regarding the reconstruction method, we showed that LSQR consistently outperforms MF
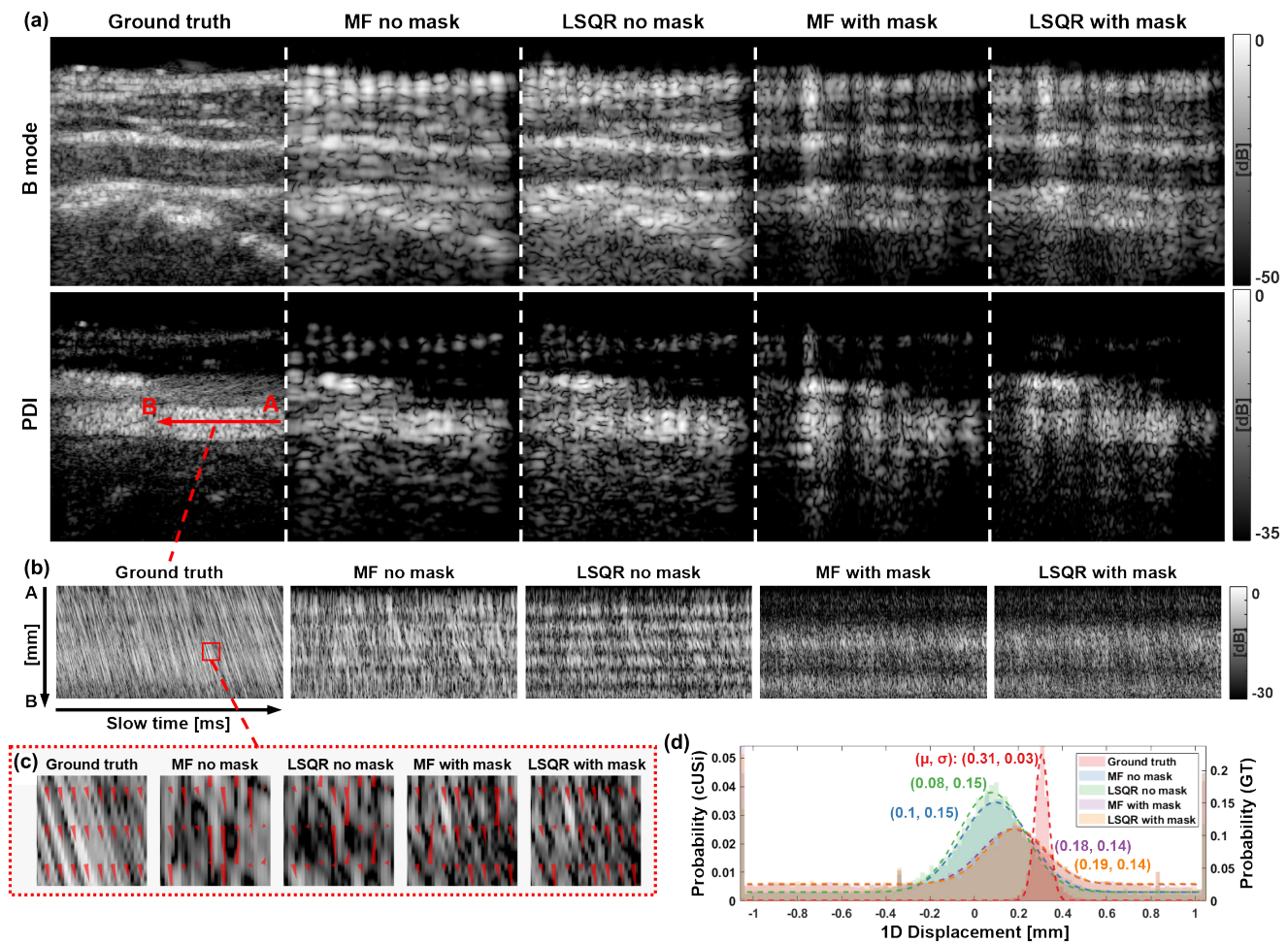
Fig. 5. CA reconstruction in the longitudinal view. (a) B-mode and PDI reconstruction of different setups. A more coherent vessel wall in B-mode and finer speckle pattern was found for the case of LSQR with mask. (b) Extracted M-mode images derived from the red line A–B in (a) show the speckle movement along the flow over the diastolic phase, and displacement is more recognizable with the mask. The 1-D speckle tracking estimation was applied (c), which also benefits from the improved blood speckle with the mask and LSQR. (d) Histogram of displacement estimation, showing results that are clearly closer to the ground truth in the cases with mask. The average speckle movement is ~0.3 mm per frame (0.2 m/s).

in terms of PSF both laterally and axially. We attribute this improvement to the better exploitation of the system matrix A in LSQR, which iteratively improves the estimated image to better fit its product with the system matrix to the received channel RF. In our emulation setup, M between 12 and 16 and D from 4 to 8 seem to give acceptable reconstruction quality for CA imaging, based on its performance in the in silico and in vitro experiments. Within this parameter range, utilizing $M = 12$ transceivers and a mask delay variation of $D = 4$ WP and LSQR reconstruction seems to reasonably compromise hardware complexity and reconstruction quality for CA B-mode imaging. This also notably enhanced PDI reconstructions, where the blood flow speckle visualization facilitated more accurate flow dynamics assessment.

Our parameter exploration was restricted in several ways. We are currently limited to a 2-D imaging domain, while we will eventually aim for a 3-D imaging approach. It is reasonable to assume that the conclusions can be extrapolated to a 3-D imaging situation, conceptualizing the 3-D system

as a stacked assembly of 2-D transceiver arrays or simply taking the square of the number of transceivers for 2-D as a first approximation for 3-D. Performing a similar emulation approach for a 3-D case is hard since we would need a 3-D fully sampled array for carotid imaging (which would require thousands of individually addressable elements). We will need to base a 3-D approach on simulations and aim to realize a prototype in forthcoming research. Preliminary evidence from our recent k Wave-based 3-D simulations supports the feasibility of such an approach with large, masked elements in a simplified CA flow model [22]. Additionally, insights gained from cUSi studies in mouse brain hemodynamics underscore the potential applicability to 3-D imaging [11], though the scale of anatomy and specific biological information sought significantly differ for CA imaging in 3-D.

In our emulation, there will be a single digital delay for each element, rather than a continuous delay pattern over the corresponding part of the larger transceiver. This spatial sampling might differ from a physical implementation. However, since we intend to use a relatively smooth encoding

mask pattern, we believe that this L7-4 transducer is sufficient for our emulation. This is supported by the results shown in Fig. 1(c).

We also applied only four-cycle tone burst transmission in all experiments. This was chosen to ensure a good SNR for LSQR, with a possible sacrifice of some axial resolution in MF reconstruction. Optimal pulselength and shape could be further investigated for different reconstruction scenarios. Besides, the lateral resolution might also vary from pulse lengths due to different interference behavior in the forward pressure field. This assumption will be investigated in future studies.

During the construction of the system model matrix, we assumed that the k-Wave simulated acoustic fields were a sufficient approximation of the real transducer elements' fields, an assumption ignoring any variations in element impulse response and sensitivity. This simplification may lead to a mismatch between the system model and practical behavior. Therefore, in the next stage of studies, we will consider using direct acoustic field measurements of all individual elements using a hydrophone for the A matrix construction, similar to what was performed in [11].

In this article, all studies were conducted using the same mask pattern to maintain comparison consistency and limit the number of free parameters. This mask was generated randomly and smoothed heuristically. Based on the findings of van der Meulen et al. [12]—which showed that random masks did not perform substantially worse than optimized masks—we assume that the influence of the mask pattern is less significant than the number of transceivers and the delay variation. During our in silico study, we observed no important differences when exploratively testing with several different mask patterns. Nevertheless, given the connection between the mask pattern and the acoustic field intensity distribution, further research would aid in defining a mask that is both acoustically efficient and practical for fabrication and implementation.

The cUSi MF reconstruction generally showed lower contrast and irregular intensity patterns induced by the inhomogeneous acoustic field distribution. This issue may be addressed by an extra postprocessing step that corrects the known transmitted pressure distribution, which would be less computationally demanding than applying LSQR. Besides, optimizing the mask pattern to achieve a more uniform pressure distribution while maintaining acoustic field spatial decorrelation could also improve the MF outcomes. The techniques based on convex optimization and random rounding, or greedy coordinate descent developed by van der Meulen et al. [12], might be exploited for our mask optimization efforts.

An SA-based transmit scheme was adopted in this article to acquire a large number of independent measurements and ensure the best reconstruction quality. However, this scheme restricts us from achieving a higher frame rate (currently 667 Hz for our in vivo experiments). Hence, only diastolic frames were used in our in vivo experiment. Future studies will focus on transmission schemes that balance image reconstruction quality, and the frame rate needed to cover the entire CA cycle, including systole.

V. Conclusion

Our research focused on finding a suitable device configuration for cUSi of the CA using a 2-D emulation system. The in silico, in vitro, and in vivo studies confirmed the improvement in reconstruction quality of applying the encoding mask and LSQR, regarding the lateral and axial PSF and CR. A cUSi device with as little as 12–16 transceivers coupled with an encoding mask with 4–8 WP delay variation appears suitable for CA monitoring. As a demonstration, high-quality B-mode and power Doppler images of the CA were successfully achieved with a setup of only 12 transceivers in conjunction with a four WP delay variation mask and LSQR reconstruction.

Acknowledgment

References

[1] E. G. Grant et al., "Carotid artery stenosis: Gray-scale and Doppler U.S. diagnosis—Society of radiologists in ultrasound consensus conference," *Radiology*, vol. 229, no. 2, pp. 340–346, Nov. 2003.

[2] W. Lee, "General principles of carotid Doppler ultrasonography," *Ultrasonography*, vol. 33, no. 1, pp. 11–17, Jan. 2014.

[3] A. A. Oglat, M. Z. Matjafri, N. Suardi, M. A. Oqlat, M. A. Abdelrahman, and A. A. Oqlat, "A review of medical Doppler ultrasonography of blood flow in general and especially in common carotid artery," *J. Med. Ultrasound*, vol. 26, no. 1, pp. 3–13, Jan. 2018.

[4] P. M. Nabeel, V. R. Kiran, J. Joseph, V. V. Abhidev, and M. Sivaprakasam, "Local pulse wave velocity: Theory, methods, advancements, and clinical applications," *IEEE Rev. Biomed. Eng.*, vol. 13, pp. 74–112, 2020.

[5] P. Kruizinga, F. Mastik, J. G. Bosch, A. F. W. van der Steen, and N. de Jong, "Carotid artery wall dynamics captured with multi-plane high-frame-rate imaging," in *Proc. IEEE Int. Ultrason. Symp. (IUS)*, Taiwan, Oct. 2015, pp. 1–4.

[6] A. Fenster, A. Landry, D. B. Downey, R. A. Hegele, and J. D. Spence, "3D ultrasound imaging of the carotid arteries," *Current Drug Targets-Cardiovascular Hematological Disorders*, vol. 4, no. 2, pp. 161–175, Jun. 2004.

[7] S.-W. Chung, C.-C. Shih, and C.-C. Huang, "Freehand three-dimensional ultrasound imaging of carotid artery using motion tracking technology," *Ultrasonics*, vol. 74, pp. 11–20, Feb. 2017.

[8] D. S. dos Santos et al., "A tiled ultrasound matrix transducer for volumetric imaging of the carotid artery," *Sensors*, vol. 22, no. 24, p. 9799, Dec. 2022.

[9] J. Provost et al., "3D ultrafast ultrasound imaging in vivo," *Phys. Med. Biol.*, vol. 59, no. 19, pp. L1–L13, Oct. 2014.

[10] P. Kruizinga et al., "Compressive 3D ultrasound imaging using a single sensor," *Sci. Adv.*, vol. 3, no. 12, Dec. 2017, Art. no. e1701423.

[11] M. D. Brown et al., "Four-dimensional computational ultrasound imaging of brain hemodynamics," *Sci. Adv.*, vol. 10, no. 3, Jan. 2024, Art. no. eadk7957.

[12] P. van der Meulen, P. Kruizinga, J. G. Bosch, and G. Leus, "Coding mask design for single sensor ultrasound imaging," *IEEE Trans. Comput. Imag.*, vol. 6, pp. 358–373, 2020.

[13] J. Janjic et al., "Structured ultrasound microscopy," *Appl. Phys. Lett.*, vol. 112, no. 25, Jun. 2018, Art. no. 251901.

[14] B. E. Treeby and B. T. Cox, "K-wave: MATLAB toolbox for the simulation and reconstruction of photoacoustic wave fields," *J. Biomed. Opt.*, vol. 15, no. 2, 2010, Art. no. 021314.

[15] N. Antipa et al., "DiffuserCam: Lensless single-exposure 3D imaging," *Optica*, vol. 5, no. 1, p. 1, Jan. 2018.

[16] J. A. Jensen, S. I. Nikolov, K. L. Gammelmark, and M. H. Pedersen, "Synthetic aperture ultrasound imaging," *Ultrason.*, vol. 44, pp. e5–e15, Aug. 2006.

[17] G. Turin, "An introduction to matched filters," *IEEE Trans. Inf. Theory*, vol. IT-6, no. 3, pp. 311–329, Jun. 1960.

[18] C. C. Paige and M. A. Saunders, "LSQR: An algorithm for sparse linear equations and sparse least squares," *ACM Trans. Math. Softw.*, vol. 8, no. 1, pp. 43–71, Mar. 1982.

[19] C. Martinoli et al., "Power Doppler sonography: Clinical applications," *Eur. J. Radiol.*, vol. 27, pp. S133–S140, May 1998.

[20] C. Demené et al., "Spatiotemporal clutter filtering of ultrafast ultrasound data highly increases Doppler and fUltrasound sensitivity," *IEEE Trans. Med. Imag.*, vol. 34, no. 11, pp. 2271–2285, Nov. 2015.

[21] Y. Notomi et al., "Measurement of ventricular torsion by two-dimensional ultrasound speckle tracking imaging," *J. Amer. College Cardiol.*, vol. 45, no. 12, pp. 2034–2041, Jun. 2005.

[22] Y. Hu et al., "3D carotid artery flow imaging using compressive sensing with a spatial coding mask: A simulation study," in *Proc. IEEE Int. Ultrason. Symp. (IUS)*, Montreal, QC, Canada, Sep. 2023, pp. 1–4.

Geert Leus (Fellow, IEEE) received the M.Sc. and Ph.D. degrees in electrical engineering from KU Leuven, Leuven, Belgium, in June 1996 and May 2000, respectively.

He is currently a Full Professor with the Faculty of Electrical Engineering, Mathematics and Computer Science, Delft University of Technology, Delft, The Netherlands.

Dr. Leus is a fellow of EURASIP. He was a recipient of the 2021 EURASIP Individual Technical Achievement Award, the 2005 IEEE Signal Processing Society Best Paper Award, and the 2002 IEEE Signal Processing Society Young Author Best Paper Award. He was a Member-at-Large of the Board of Governors of the IEEE Signal Processing Society, the Chair of the IEEE Signal Processing for Communications and Networking Technical Committee, the Chair of the EURASIP Technical Area Committee on Signal Processing for Multisensor Systems, and the Editor-in-Chief of the *EURASIP Journal on Advances in Signal Processing*. He is currently the Editor-in-Chief of *EURASIP Journal on Advances in Signal Processing*.

Yuyang (FOX) Hu (Student Member, IEEE) received the bachelor's and master's degrees in biomedical engineering from Shenzhen University, Shenzhen, China, in 2011 and 2019, respectively. He is currently pursuing the Ph.D. degree with the Thoraxcenter Biomedical Engineering Group, Department of Cardiology, Erasmus University Medical Center, Rotterdam, The Netherlands.

His research is about applying computational ultrasound imaging for carotid artery monitoring with a low number of sensors.

Antonius F. W. van der Steen (Fellow, IEEE) received the M.Sc. degree in applied physics from Technical University Delft, Delft, The Netherlands, in 1989, and the Ph.D. degree in medical science from Catholic University Nijmegen, Nijmegen, The Netherlands, in 1994.

He is currently the Head of biomedical engineering with the Thorax Center, Erasmus University Medical Center, Rotterdam, The Netherlands. He is an Expert in ultrasound, cardiovascular imaging, and cardiovascular biomechanics. He has a career at the crossroads of engineering, health care, and industry. He was the Co-Principal Investigator of ParisK, one of the large CTMM projects (16 MEuro). His international profile is high, with more than 200 invited lectures all over the world, and Guest Professorship/Guest Researcher in Canada, Japan, and China.

Dr. van der Steen is a fellow of European Society of Cardiology. He is a member of the Netherlands Academy of Technology (AcTI) and a Board Member of the Royal Netherlands Academy of Sciences (KNAW). He was a recipient of the Simon Stevin Master Award and the NWO PIONIER Award in Technical Sciences. He has experience in running large consortia as the Co-Founder and former Chairperson of the Medical Delta, which comprises more than 280 scientists working on technical solutions for sustainable health.

Didem Dogan (Member, IEEE) received the M.Sc. degree in electrical engineering from Middle East Technical University, Ankara, Türkiye, in 2020. She is currently pursuing the Ph.D. degree with the Signal Processing Systems Department, Delft University of Technology, Delft, The Netherlands.

Her research interests include the general area of signal processing, with an emphasis on computational imaging and particularly ultrasound imaging.

Pieter Kruizinga (Member, IEEE) received the Ph.D. degree from the Erasmus MC University Medical Center, Rotterdam, The Netherlands, in 2015.

In 2018, he joined the Neuroscience Department, Erasmus University Medical Center, where he leads the imaging research with the Center for Ultrasound and Brain-Imaging Erasmus MC (CUBE). His current research focuses on computational ultrasound imaging and functional ultrasound imaging of the brain.

Michael Brown (Member, IEEE) received the M.Sc. degree in physics from the University of Bristol, Bristol, U.K., in 2012, and the M.Res. degree in medical and biomedical imaging and the Ph.D. degree from University College London (UCL), London, U.K., in 2014 and 2018, respectively.

He is currently a Postdoctoral Research Fellow with the Department of Medical Physics and Biomedical Engineering, UCL, and the Department of Neuroscience, Erasmus University Medical Center, Rotterdam, The Netherlands. His research interests are methods for ultrasound wavefront shaping and computational and functional imaging.

Johannes G. Bosch (Member, IEEE) received the M.Sc. degree in electrical engineering from Eindhoven University of Technology, Eindhoven, The Netherlands, in 1985, and the Ph.D. degree from Leiden University Medical Center, Leiden, The Netherlands, in 2006.

He is currently an Associate Professor and a Staff Member with the Thoraxcenter Biomedical Engineering, Department of Cardiology, Erasmus University Medical Center, Rotterdam, The Netherlands. His research interests include 2-D and 3-D echocardiographic image formation and processing, transducer development, and novel ultrasound techniques for image formation and functional imaging.